Sensors and Materials, Vol. 34, No. 7 (2022) 2879–2895
MYU Tokyo

S & M 3012

Adaptive Region of Interest Detection Method for Liver Cancer Image Based on Convolutional Neural Network for Biochemical Sensing System

Shaohu Gu*

Changsha Aeronautical Vocational and Technical College, Hunan 410124, China

(Received April 1, 2022; accepted May 30, 2022)

Keywords: convolutional neural network, ROI, histogram equalization, loss function, biochemical sensing system

Traditional image-based detection methods for liver cancer have problems of large overlap error and low accuracy; thus, a paradigm based on the overlapping error for image detection has been proposed in previous works. In addition, biochemical sensing systems, such as lab-on-a-chip, BioMEMS/NEMS, and biomimetic systems, have stimulated much interest in the research community. We propose an adaptive region of interest detection method based on a convolutional neural network. Deep learning is carried out for some layers of the convolutional neural network, and parameters are optimized by using the improved loss function. Image features are enhanced and extracted in combination with histogram equalization, liver cancer regions of interest are extracted on the basis of an extensible markup language file, and the adaptive detection of liver cancer shadow-related areas is completed via computing through online detection and annotating a sequence of computed tomography images. Experimental results show that the proposed algorithm can effectively reduce the overlap error and improve the detection accuracy. When the number of image sets was 300, the detection accuracy of this method was 95.5%.

1. Introduction

The liver is one of the most important organs of the human body, and early effective pathological detection can help treatment. To help medical experts diagnose and treat liver diseases, it is necessary to accurately segment the region of interest (ROI) of liver cancer on a computed tomography (CT) image.(1) The liver is composed of hepatic lobules and liver cells, but the image boundary information is not accurate owing to the use of different scanning instruments. To help clinical experts diagnose and treat liver cancer, it is necessary to accurately detect the feature information in CT images.(2,3) The accurate segmentation of liver cancer tissue from CT images has been a research hotspot in recent years. To solve this problem, a variety of liver cancer image detection methods have been proposed.(4) Among them, common methods include gray level and gradient feature information detection methods, the level set method, and

*Corresponding author: e-mail: shaohugu@163.com
https://doi.org/10.18494/SAM3929

ISSN 0914-4935 © MYU K.K.
https://myukk.org/

the graph cut method. The working principle of the methods based on gray information is to check the image target intuitively and define the image boundary information according to the gray value of the image. However, such methods are limited by the gray distance between the background and the target. When the gray distance of the target is very long, the performance of image target detection is poor. For some liver cancer images with an uneven gray distribution, undersegmentation and overcutting occur during detection. In addition, a statistical segmentation method based on shape has been proposed. Whether these two methods can accurately detect the ROI in a liver image mainly depends on the liver image registration process. However, because of the close relationship between human liver images and other tissue texture images, the registration process has low performance. Therefore, a method that can automatically detect and accurately obtain image features of liver cancer is urgently required.

Sun *et al.* proposed a liver cancer detection method based on the polarization characteristics of biological tissue, i.e., the principle of interaction between light and biological tissue. They used a polarization imaging system for 30-μm-thick dyeing, not a hepatocellular carcinoma (HCC) slice image, to characterize the structure of biological tissue.[5] This method can improve the effectiveness of pathological detection, but the detection accuracy still requires improvement. Guo *et al.* proposed a detection method for liver tumors and pulmonary nodules based on medical CT images.[6] In this method, liver tumors and pulmonary nodules were detected by deep learning and lung nodules were detected by the target detection method.

To detect liver lesions more accurately and effectively, in this paper, we propose an adaptive ROI detection method based on a convolutional neural network (CNN). In particular, we constructed a network model for the automatic detection of liver cancer images, then completed the network model depth learning, e.g., optimizing the model parameters, uniting histogram equalization, extracting image features, as well as obtaining ROI information for liver cancer. Finally, a method involving CT sequence online detection and labeling is applied, and the adaptive detection of liver cancer shadow-related areas is completed. Simulation results show that the algorithm can effectively reduce the volume overlap error and improve the detection accuracy.

2. Network Architecture for Automatic Detection

2.1 Convolutional neural network

The overall structure of a CNN is very similar to that of a feedforward neural network. Similarly to a feedforward neural network, each node in a CNN is a neuron.[7–9] Figure 1 shows the structure of a CNN.

(1) Input layer

The input layer inputs information into the neural network, which provides image data to the network. The working principle of this layer is to convert the 3D matrix data in the image into the input matrix of the neural network and then transmit the input matrix to the convolution layer through the link transmission.

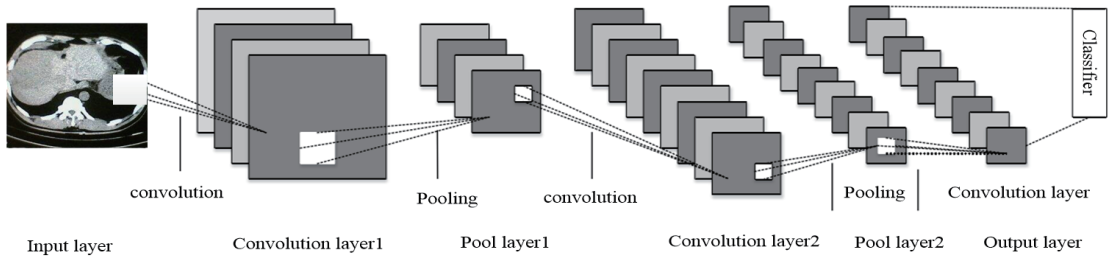

Fig. 1. Structure of CNN.

(2) Convolution layer

The convolution layer is the most important layer in the CNN, and the convolution layer filter is the core part of the network, also known as the core. Figure 2 shows the structure of the CNN test network considered in this paper.

The convolution layer filter calculates the element matrix node of the lower bit element by using the propagation structure via the kernel. The calculation formula of the lower element is

$$C(B) = f\left(\sum_{a=1}^{1} \sum_{b=1}^{1} \sum_{c=1}^{4} q_{a,b,c} \lambda_{a,b,c}^{n} \right), \tag{1}$$

where $q_{a,b,c}$ is the node value, $\lambda_{a,b,c}^{n}$is the weight of node n, and v is the bias parameter. The CNN uses matrix multiplication to establish the relationship between the input and the output. Each parameter in the weight matrix represents the relationship between the input value and the output unit.[10,11]

(3) Pool layer

This method reduces the dimension of each feature map and the size of the matrix while retaining the most important information in the feature graph.[12] The pooling layer operated with the maximum value is called the maximum pool layer, and the pooling layer operated with the average value is called the average pool layer. The filter is also in the pooling layer. Although there is still a convolution depth in a single-layer filter, the depth layer still exists and the span of the filter is only one. The movement of the filter layer in the pooling is affected by the length, width, and depth of the tank.

2.2 Parameter optimization algorithm

In the training process, the gradient descent method is used for optimization, and the loss function of the gradient descent algorithm is given. In the training process, the loss function is used to evaluate the quality and applicability of the model.[13–15] The model in this paper has a smaller loss function, a better fitting degree, and better parameters than the gradient descent method. In this paper, the normalized exponential function is used as the loss function.

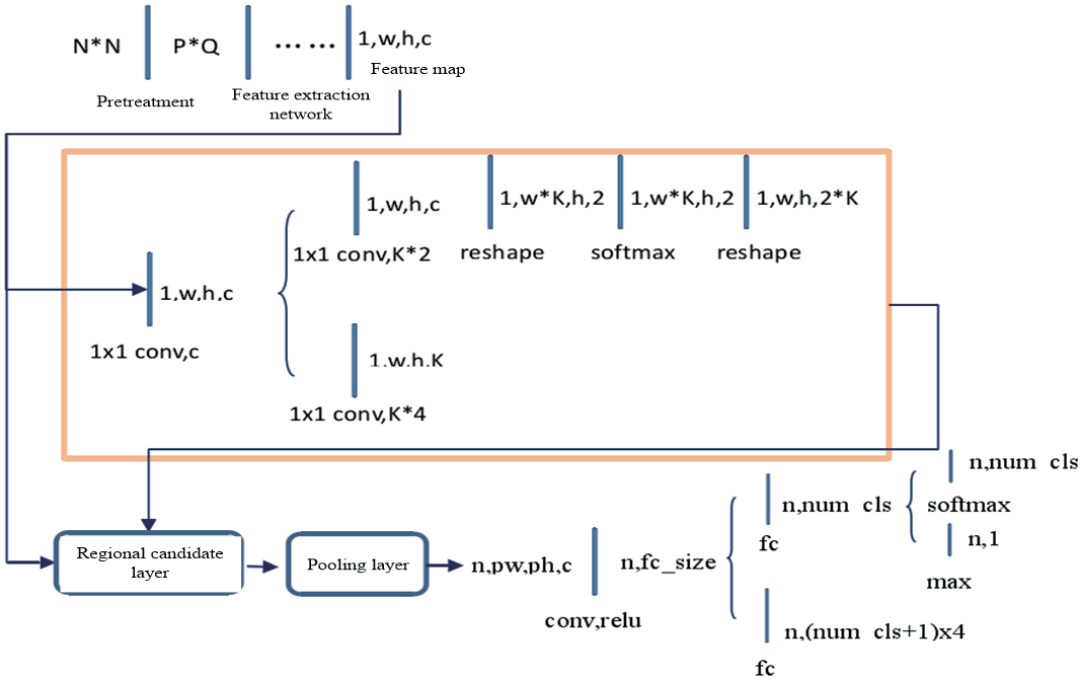

Fig. 2. (Color online) Structure of CNN test network.

$$S(x) = \frac{e^{x_i}}{\sum_{i=1}^{m} e^{x_i}} \tag{2}$$

It can be seen from Eq. (2) that through the normalized exponential function, the sum of all input values is 1, that is, each input value is the probability of a specific category. The formula used to update the parameters in the gradient descent direction is

$$x'_i = x_i - \alpha \frac{\partial C(B)}{\partial x_i}, \tag{3}$$

where α is the learning step size and determines the length of each step in the gradient descent process. The parameters are updated until the loss function achieves the minimum value.

3. Liver Cancer Image Preprocessing and Sample Acquisition Based on Histogram Equalization

In this section, we study the liver cancer image preprocessing and sample acquisition methods. The process used to construct the database is shown in Fig. 3.

The CT images of liver cancer are stored in DICOM format, making it necessary to analyze the CT images and transform them into gray images. To extract the ROI, the extensible markup language (XML) annotation file in the database provided by experts is used to extract

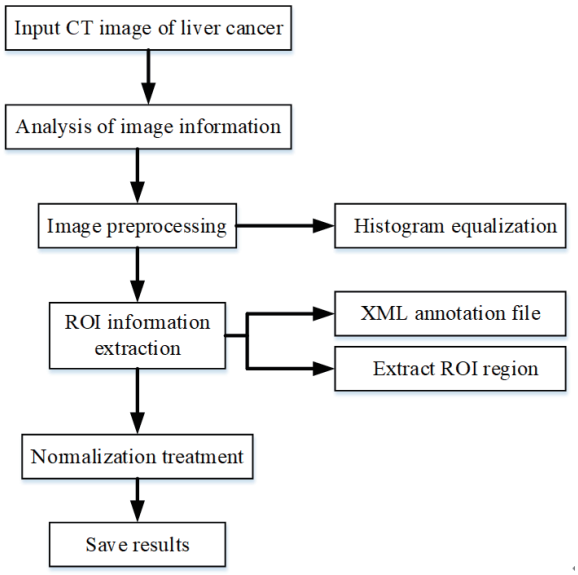

Fig. 3. Construction process for database of liver cancer image samples.

coordinated decisions on liver cancer. Finally, the ROI is standardized to establish a unified liver cancer image sample database.

3.1 Enhancement of liver cancer image based on histogram equalization

Histogram equalization is a process of improving the overall image contrast by adjusting the direct distribution of the image gray level.[16] The process can make the gray level on the histogram more uniform, which is conducive to improving the contrast of the image. It is particularly suitable for the background and foreground of medical images, i.e., light-dark contrast.[17]

Histogram equalization involves mapping and transforming the gray level of the original image, i.e., transforming the gray value R into $S = T(R)$. The probability density function $G(R)$ is used to represent the gray level distribution of the image, and $T(R)$ is the transformed gray level function,

$$S = T(R) = \int_0^R G(R)dR, \tag{4}$$

where $0 \leq R \leq 1$.

3.2 Extraction of liver cancer candidate region based on XML file

The 2D CT findings of HCC and other liver tissues are collectively referred to as liver lesions. To obtain the ROI of liver cancer, an accurate segmentation of the liver cancer is required in traditional liver cancer detection, for which the process is complex.[18] In this paper, we propose a new method of selecting candidate regions by combining two schemes.

(1) The edge detection algorithm obtains the edge region of the CT image.

(2) The 2D Gaussian function probability threshold method fine-tunes the edge region.

Two thousand candidate points are obtained by the two schemes, in which three scale candidate regions are formed. This method is targeted and can cover the liver cancer site comprehensively.[19,20] A 2D Gaussian probability density function of the liver disease template is constructed:

$$M(x,y)=\frac{\rho\left(\frac{x-\mu_1}{\sigma_1}-\frac{x-\mu_2}{\sigma_2}\right)^2}{2\pi\sigma_1\sigma_2\sqrt{1-\rho}}, \tag{5}$$

where μ_1 and μ_2 are expected values and σ_1 and σ_2 are variances. When $\rho \geq 1$, a high-response region is generated in the middle of the 2D image, as shown in Fig. 4.

Figure 4(a) shows the original input of the CT image, Fig. 4(b) shows the high-response region of the 2D Gaussian function on the left side of the 2D image, Fig. 4(c) shows the edge sampling point generated by Carney edge detection, and Fig. 4(d) shows the 2000 sampling areas generated by the two methods. To make full use of the spatial context information of CT sequences, positive predictive values are added to the sequences as candidate seed points.[21] In the online test, the generated sampling area is used as the input area for target classification and the detection of CT images. The selected scale area contains three scale images centered on seed points.

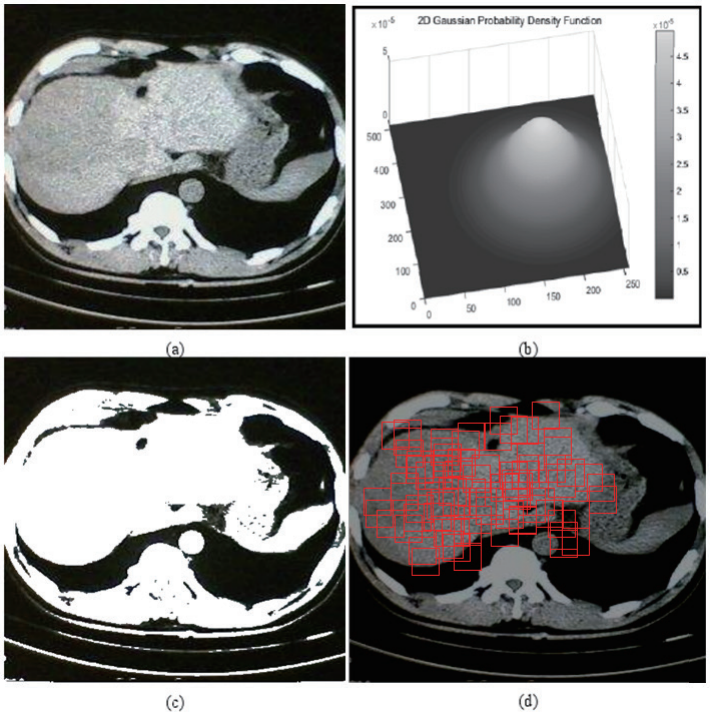

Fig. 4. (Color online) Schematic diagram of candidate area.

The main bases of target recognition and classification are the texture and contour features of the ROI. According to the feature information of CT images, three types of image data are constructed as the original input.

(1) After adjusting the window width and window height, the CT gray image is used by doctors to determine the type of disease.
(2) A gray enhanced image, which emphasizes the target, strengthens the contrast between the target and the background, and highlights the characteristics of the target.
(3) The scanned image obtained by the CT machine and the original CT value can reflect the ability of X-rays to penetrate human tissue, and the clarity and range slightly depend on the radiation dose intensity.

High-density tissue has a radiodensity between −1000 and +1000 Hu, and the penetration ability of X-rays is weak. The segmentation range of the CT value increases the difference between different tissues, making it easy to distinguish them.[22–24] The problem with large-scale segmentation is that the image cannot be directly represented, although the data is still valuable, as shown in Fig. 5.

On the basis of the above contents, the liver cancer information in the XML file is analyzed and extracted as follows.

(1) Calculate the patient's number. Set the string of intervals as the number information of patients.
(2) Extract the labeling information of four radiologists by a circulation method.

XML file and annotation information corresponding to four experts is obtained. If the expert's number is not given in the XML file, it is necessary to perform the following steps at each interval:

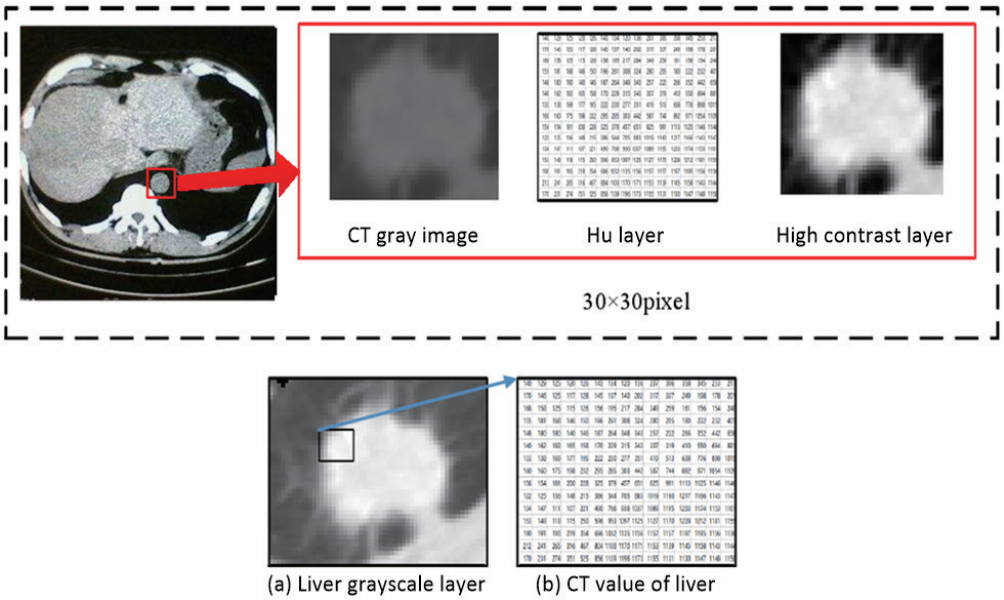

Fig. 5. (Color online) Liver CT data.

(1) Search for tags that store liver cancer information. When the tags contain effective markers, the feature information of subjective lesions can be extracted. In addition, all liver cancer coordinate information is saved on each label.
(2) Search for tags for non-liver cancer information.

Using the above XML file parsing steps, we obtain the information from all liver cancer and non-liver cancer radiologists. This method is based on liver cancer and non-liver cancer coordinates, and the information is accurate and reliable. The ROI region is selected from liver CT images of the corresponding patients.[25] In addition, the CNN works well in the case of a background without the need for the accurate segmentation of liver cancer.

3.3 ROI extraction

ROI extraction can greatly shorten the image processing time, improve the accuracy of subsequent classification, and greatly increase convenience in image analysis.[26] In this study, we use the morphological method to separate the ROI, which improves the effectiveness of detection for the subsequent image classification. For liver CT images, it is unnecessary to take the whole image as the input data for deep learning; only the ROI must cover the liver cancer area.[27] The processing steps are as follows:

After the image is processed, noise such as the scan line is removed. Then, the image template is obtained by hole filling and mask operations, and the ROI of the liver cancer image is obtained by a mask operation.[28] After detection and segmentation, the image can be used as the input image of the model for recognition, but the general recognition of liver cancer mainly focuses on the ROI. Therefore, it is necessary to continue using the threshold and morphological methods to extract the ROI from the segmented image to eliminate the interference of small human tissues and blood vessels.

3.4 Achieving normalized samples

Because of the different sizes of ROI regions, the size of the input image in the network model must be consistent to avoid large errors in the detection results. Bilinear interpolation is used to standardize the ROI. The algorithm ensures that the enlarged image maintains continuous pixel values in the *X*- and *Y*-directions to ensure the image quality.

Figure 6 shows a schematic of the bilinear difference algorithm. Linear interpolation is carried out for the sum in the *X*-direction. The gray value after interpolation is given by Eqs. (6) and (7):

$$f(L_i) = \frac{x_{i+1} - x}{x_{i+1} - x_i} f(Z_{ij}) + \frac{x - x_i}{x_{i+1} - x_i} f(Z_{i+1\,j}), \tag{6}$$

$$f(L_{i+1}) = \frac{x_{i+1} - x}{x_{i+1} - x_i} f(Z_{ij+1}) + \frac{x - x_i}{x_{i+1} - x_i} f(Z_{i+1\,j+1}). \tag{7}$$

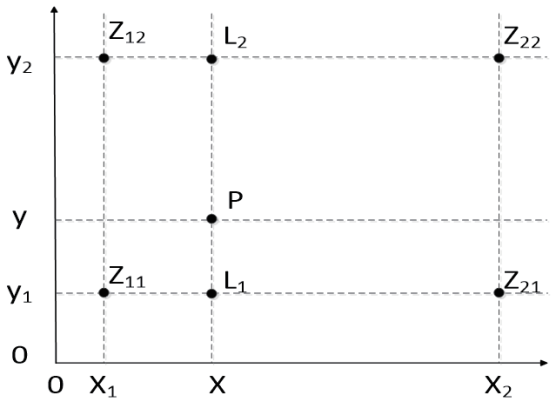

Fig. 6. Bilinear interpolation method.

Then, linear interpolation is carried out in the *Y*-direction using L_i and L_{i+1}. The gray value after interpolation is as follows:

$$H(x)=\frac{y_{i+1}-x}{y_{i+1}-x_i}f(L_i)+\frac{y-y_i}{y_{i+1}-y_i}f(L_{i+1}), \tag{8}$$

where $H(x)$ is the pixel value after bilinear interpolation. In this paper, the bilinear interpolation algorithm is used to normalize the extracted candidate region and convert it into a 32 × 32 image.

4. Adaptive ROI Detection Method for Liver Cancer Image Based on CNN

4.1 Strategy for improving the CNN model

We complete the detection of the liver cancer ROI by using a 2D segmentation image. Because of the time and the large amount of memory required for the training process, for the extracted part, the target can be reduced to the size of the liver cancer.

The pixel center of the 2D candidate is taken as the centroid, and two fixed-size custom pixels are extracted as the training set of the classification network. In this method, two blocks (25 × 25 × 8 and 50 × 50 × 20) are extracted to train two different volume integral networks. Compared with traditional methods, this method has three advantages:

(1) For liver cancer with a large diameter, this method contains all the information about the liver and avoids the problem of incomplete information due to the set size of a single scale being very small.
(2) For liver tumors with a small diameter, this method maintains a large proportion of small slices to ensure that the network learns useful features.
(3) This method increases the amount of context-aware information in the classification process and improves the recognition accuracy of the classification model.

4.2 Online detection and labeling of CT sequences

To make full use of the spatial information in the detection process and detect the complete image, we propose a CT layer-by-layer detection method based on the complete sequence. By predicting the neighborhood of the CT sequence, a highly responsive voxel space is obtained, thus realizing the online detection and annotation of the sequence.[29,30] The sequence line detection method can improve the detection accuracy and reduce false alarms. In the detection process, a CNN with the same structure as in Fig. 1 is used for detection. The final test results $y(Y_1, Y_2, Y_3)$ are generated by a voting mechanism.

To ensure a large number of training data and testing data processing under the condition of large-scale data, the image is adjusted to three scales of 102, 202, and 302 pixels.[31,32] Aiming at the selection of the interpolation method, we propose an optimization algorithm based on gray image information entropy. For a gray image, the information entropy is expressed as

$$S_x = \sum_{i=0}^{\max} k_i \lg k_i, \tag{9}$$

where k_i is the probability value of pixels in the image.

4.3 Adaptive detection results

For candidate nodule u_i, different classification results are recorded as $P_1(I = k \mid u_i)$ and $P_2(I = k \mid u_i)$, where the former with $k = 0$ is the probability of a non-nodule and the latter with $k = 1$ is the probability of a nodule. In this study, we detect the output of the network model adaptively. The formula used in adaptive fusion detection is

$$R(h) = \tau \frac{\sum_{i=1,2} w_i P_i}{S_x}, \tag{10}$$

where τ is the adaptive learning step size and w_i is the corresponding weight of each classification result. To verify the effectiveness and feasibility of this method, we carried out simulation experiments.

5. Implementation and Verification of Detection Algorithm

5.1 Experimental platform

The computer configuration used in this experiment was composed of the following components: inteli7-8700 CPU, NVIDIA GTX 1060 GPU, 6 GB video memory, 16 GB memory configuration, Linux operating system, Ubuntu 14.04, deep learning framework for Caffe, CUDA, OpenCV, and Blas, and Python and MATLAB programming languages.

5.2 Experimental data

The data set used was from TCGA, the largest publicly available reference database of tumor genomic maps, which contains 1634 CT scans. The resolution of each slice is 512 × 512 and the element spacing is 0.74–0.742 mm.

The data included DICOM medical images and annotated information from four radiologists, who annotated the dataset in two phases. Each expert determined the characteristics of the lesion in the first stage, then examined the results of the other three experts in the second stage to determine the final diagnosis. On this basis, after two stages of processing, the rate of missed diagnosis was minimized, giving the data set a high reference value. The data also included the degrees and characteristics of the lesions.

For subjective reasons, different experts made different comments on the same images. Taking the comments of 3–4 experts as the final reference standard, 500 CT examination results were used as experimental data. During the experiment, the data set was divided into the training and test sets, and the 50-fold cross-validation method was used. Five hundred CT scan results were randomly divided into five groups. In the experiment, four groups were selected as the training set and the fifth group was selected as the test set. Therefore, different datasets were obtained each time, ensuring the full use of samples and accurate results.

5.3 Parameter setting

In the training process, the pre-trained model was used for retraining. The weight of each CNN layer was determined by the random gradient descent method. The standard deviation of the weight was 0.0105. The batch setting was 12, the momentum was 0.9, the weight attenuation was 5×10^{-4}, and the initial learning rate was 10^{-4}.

5.4 Evaluation index

(1) Volumetric overlap error

The smaller the error between the actual and expected segmentation result volumes, the more accurate the liver segmentation result. The volumetric overlap error is defined as

$$V(i) = 1 - \frac{|A \cap B|}{|A \cup B|}, \tag{11}$$

where A is the area of liver cancer in the detection result and B is the expected detection result. The test results are shown in Fig. 7 and Tables 1–3.

It can be seen from the results that the error of the proposed method is the smallest among the methods, i.e., information about liver cancer is detected the most accurately.

(2) Receiver operating characteristic (ROC) curve analysis

In the working characteristic curve of a research object, the false positive (FP) is plotted on the horizontal axis and the true positive (TP) is plotted on the vertical axis. In the field of disease

(a) (b) (c)

Fig. 7. (Color online) Liver cancer detection results. (a) Original picture. (b) Actual liver cancer area. (c) Method of this paper.

Table 1
Results of the method of this paper.

Frequency	Volume overlap error (%)
50	5.34
100	5.46
150	5.87
200	5.55
250	5.31

Table 2
Results of liver imaging using method in Ref. 5.

Frequency	Volume overlap error (%)
50	7.33
100	6.45
150	7.31
200	7.56
250	6.99

Table 3
Results of liver imaging using method in Ref. 6.

Frequency	Volume overlap error (%)
50	36
100	35.98
150	37.01
200	34.56
250	36.12

diagnosis, the ROC curve is widely used, which can effectively demonstrate the ability of different detection methods in disease differentiation. It can intuitively and concisely analyze the accuracy of images and reveal the relationship between sensitivity and specificity. The ROC curves obtained by image processing using different methods are shown in Fig. 8.

As can be seen from Fig. 8, the image input model after image preprocessing in this paper has a higher recognition performance than that in Refs. 5 and 6.

The ROC curves after image processing are higher than those for the original image. However, this method is very effective when the specificity exceeds 0.2. The closer the specificity is to exceeding 0.2 in the ROC curve, the more effective the method will be. The results show that the model has a high recognition rate after segmentation and ROI extraction, which is conducive to improving the classification accuracy of the model.

To verify the effectiveness of different detection methods for liver cancer images, the methods in Refs. 5 and 6 and the proposed method are compared in terms of the highest detection accuracy for different image sets, and the results are shown in Table 4.

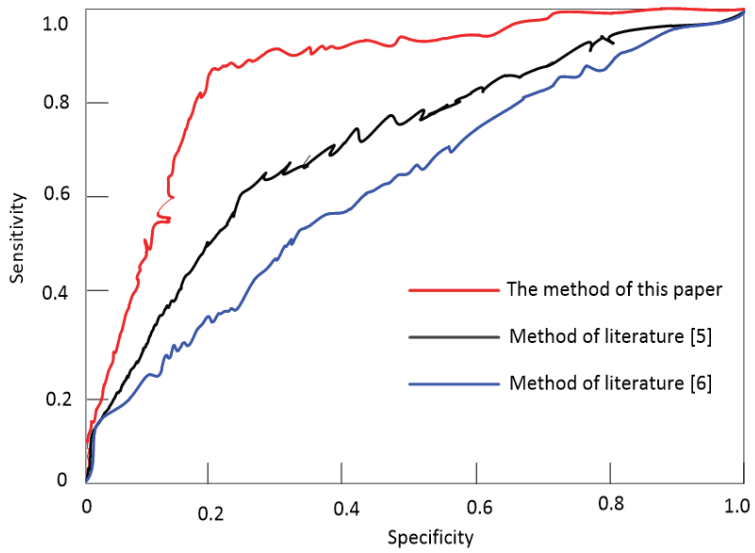

Fig. 8. (Color online) ROC curves.

Table 4
Highest detection accuracies of different methods.

Number of image sets	Highest detection accuracy (%)		
	Method in Ref. 5	Method in Ref. 6	Proposed method
50	76.0	80	98.0
100	78.0	78	98.0
150	74.0	75.6	97.0
200	72.0	73.4	96.5
250	69.5	70.2	96.0
300	68.2	69.8	95.5

The highest detection accuracy of the proposed method in this paper is significantly greater than those of the other methods for all numbers of image sets. Thus, the proposed method has high detection accuracy and applicability.

(3) Performance comparison of different computer-aided design systems

To verify the performance of the proposed method and the methods in Refs. 5 and 6, we compared all the network models and obtained the accuracy rate for liver image segmentation in the training and testing sets, as shown in Figs. 9 and 10, respectively.

The experimental results show that the indexes of the proposed method are better than those of the two methods. In CT images, blood vessels, tissues, and fat have little effect on model recognition, making it necessary to preprocess the CT images. Using the morphological method to reconstruct the image, targeting the small noise and concave defects at the edge of the image, the noise interference is reduced, which is conducive to improving the classification effect of the model and further improving the accuracy of detecting liver images.

To evaluate the effectiveness of image detection for liver cancer lesions for the three methods, we obtain the image detection results for liver cancer lesions shown in Fig. 11.

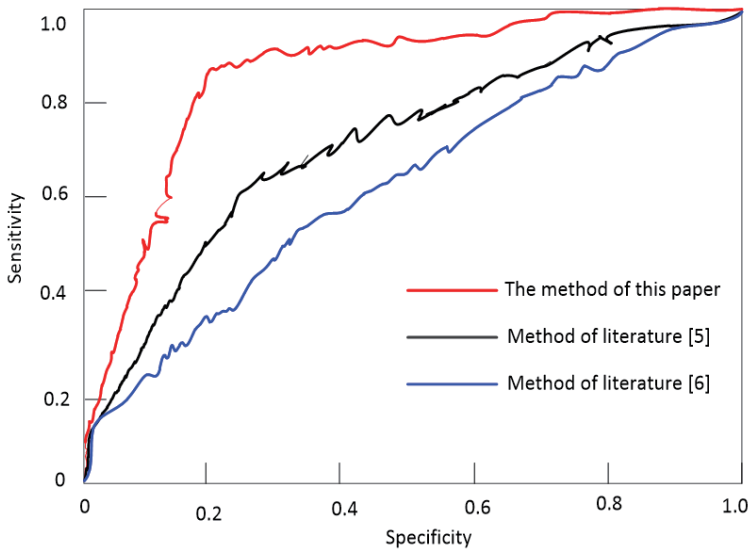

Fig. 9. (Color online) Accuracy of each algorithm for the training set.

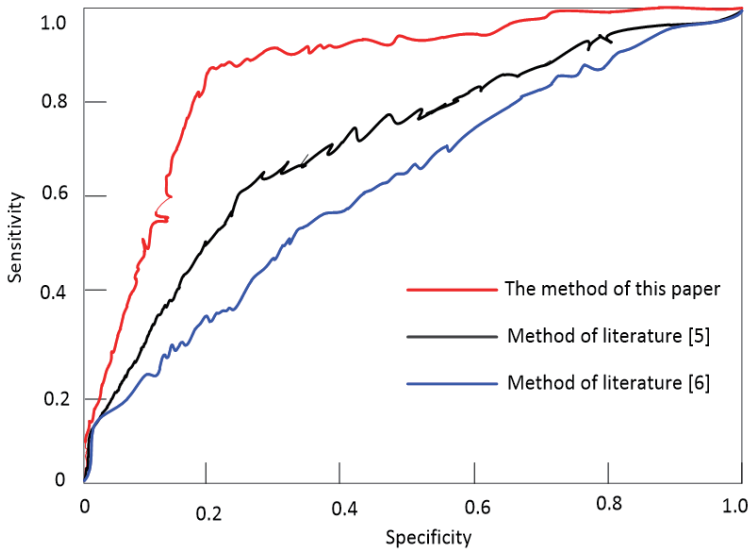

Fig. 10. (Color online) Accuracy of each algorithm for the testing set.

In Fig. 11, the red box indicates the bounding box predicted to be a liver cyst lesion, and the character set Cyst 1.00 indicates that the predicted probability of the lesion being a cyst is 1.00. The green box and data indicate the bounding box of the labeled lesion and the type of lesion, respectively. Figure 11 shows that the detection results for liver cyst lesions are different for the different methods. It can be seen from this figure that the proposed method has the highest accuracy rate.

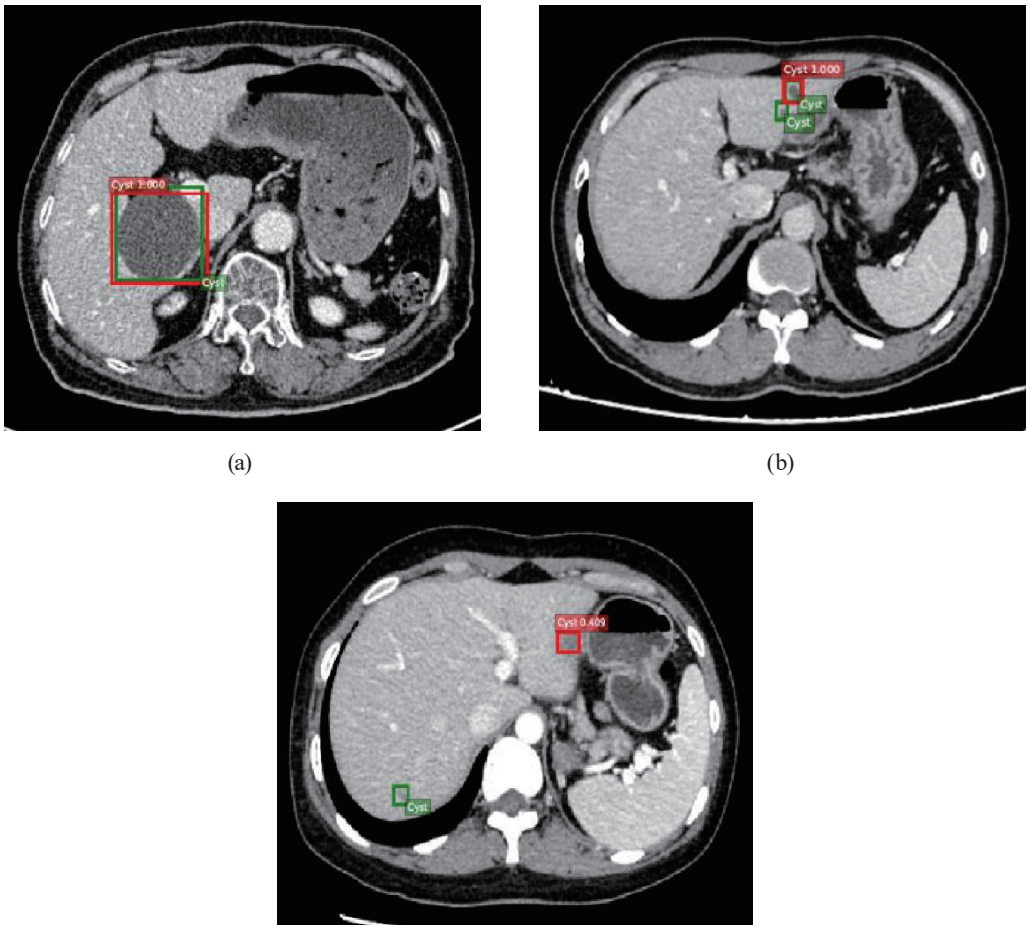

(a) (b)

(c)

Fig. 11. (Color online) Image detection results of liver cancer lesions for different methods. (a) Proposed method, (b) method in Ref. 5, and (c) method in Ref. 6.

6. Conclusions

The ROI is an important tool for doctors to diagnose HCC. To solve the problems of volume overlap error and low accuracy of traditional liver cancer image detection methods, an adaptive ROI detection method based on a CNN was proposed. Through several sets of comparative experiments, we demonstrated that the performance of the proposed method is superior to that of traditional methods. Although there are still some shortcomings in the proposed method, it can also be applied to other image data and medical image processing tasks.

Acknowledgments

This work was supported by a scientific research project of Hunan Education Department (No. 21C1560).

References

1 Y. S. Kim, D. Wu, K. Gong, J. Dutta, J. H. Kim, Y. D. Son, H. K. Kim, G. E. Fakhri, and Q. Li: IEEE Trans. Med. Imaging **37** (2018) 1478. https://doi.org/10.1109/TMI.2018.2832613
2 T. C. Chiang, Y. Huang, R. Chen, C. Huang, and R. Chang: IEEE Trans. Med. Imaging **38** (2018) 240. https://doi.org/10.1109/TMI.2018.2860257
3 M. Winkels and T. S. Cohen: Med. Image Anal. **55** (2019) 15. https://doi.org/10.1016/j.media.2019.03.010
4 M. Z. Alom, C. Yakopcic, M. S. Nasrin, T. M. Taha, and V. K. Asari: J. Digit. Imaging **32** (2019) 605. https://doi.org/10.1007/s10278-019-00182-7
5 C. Sun, A. Xu, D. Liu, Z. Xiong, F. Zhao, and W. Ding: IEEE J. Biomed. Health **24** (2020) 1643. https://doi.org/10.1109/JBHI.2019.2949837
6 Z. Guo, X. Li, H. Huang, N. Guo, and Q. Li: IEEE Trans. Radiat. Plasma Med. Sci. **3** (2019) 162. https://doi.org/10.1109/TRPMS.2018.2890359
7 J. Jiang, Y. Hu, C. Liu, D. Halpenny, M. D. Hellmann, J. O. Deasy, and G. Mageras: IEEE Trans. Med. Imaging **38** (2019) 134. https://doi.org/ 10.1109/TMI.2018.2857800
8 Z. Zhou, M. M. R. Siddiquee, N. Tajbakhsh, and J. Liang: IEEE Trans. Med. Imaging **39** (2020) 1856. https://doi.org/10.1109/TMI.2019.2959609
9 X. Ren, L. Xiang, D. Nie, Y. Shao, H. Zhang, D. Shen, and Q. Wang: Med. Phys. **45** (2018) 2063. https://doi.org/10.1002/mp.12837
10 S. Eloot, Y. D'asseler, P. D. Bondt, and P. Verdonck: Int. J. Artif. Organs. **28** (2005) 739. https://doi.org/10.1177/039139880502800713
11 P. B. Zanzonico: Health Phys. **116** (2019) 135. https://doi.org/10.1097/HP.0000000000001038
12 A. Kumar, M. Fulham, D. Feng, and J. Kim: IEEE Trans. Med. Imaging **39** (2020) 204. https://doi.org/10.1109/TMI.2019.2923601
13 E. Kang, W. Chang, J. Yoo, and J. Ye: IEEE Trans. Med. Imaging **37** (2018) 1358. https://doi.org/10.1109/TMI.2018.2823756
14 H. Shan, Y. Zhang, Q. Yang, U. Kruger, M. K. Kalra, L. Sun, W. Cong, and G. Wang: IEEE Trans. Med. Imaging **37** (2018) 1522. https://doi.org/10.1109/TMI.2018.2832217
15 N. Pietro, J. C. Daniel, B. P. David, R. W. George, N. R. Farbod, J. L. C. Maria, and R. S. J. Estépar: IEEE Trans. Med. Imaging **37** (2018) 2428. https://doi.org/10.1109/TMI.2018.2833385
16 R. A. Lobos, T. H. Kim, W. S. Hoge, and P. H. Justin: IEEE Trans. Med. Imaging **37** (2018) 2390. https://doi.org/10.1109/tmi.2018.2822053
17 L. Li, M. Xu, H Liu, Y. Li, X. Wang, L. Jiang, Z. Wang, X. Fan, and N. Wang: IEEE Trans. Med. Imaging **39** (2020) 413. https://doi.org/10.1109/TMI.2019.2927226
18 M. Li, W. Hsu, X. D. Xie, J. Cong, and W. Gao: IEEE Trans. Med. Imaging **39** (2020) 2289. https://doi.org/10.1109/TMI.2020.2968472
19 W. Li, J. Li, K. Sarma, K. C. Ho, S. Shen, B. S. Knudsen, A. Gertych, and C. W. Arnold: IEEE Trans. Med. Imaging **38** (2019) 945. https://doi.org/10.1109/TMI.2018.2875868
20 J. Tan, Y. Gao, Z. Liang, W. Cao, M. J. Pomeroy, Y. Huo, L. Li, M. A. Barish, A. F. Abbasi, and P. J. Pickhardt: IEEE Trans. Med. Imaging **39** (2020) 2013. https://doi.org/10.1109/TMI.2019.2963177
21 X. Xu, F. Zhou, B. Liu, D. Fu, and X. Bai: IEEE Trans. Med. Imaging **38** (2019) 1885. https://doi.org/10.1109/TMI.2019.2894854
22 J. Hu, Y. Chen, J. Zhong, R. Ju, and Z. Yi: IEEE Trans. Med. Imaging **38** (2018) 269. https://doi.org/ 10.1109/TMI.2018.2863562
23 H. Huang, X. Hu, Y. Zhao, M. Makkie, Q. Dong, S. Zhao, L. Guo, and T. Liu: IEEE Trans. Med. Imaging **37** (2018) 1551. https://doi.org/10.1109/TMI.2017.2715285
24 M. Zreik, R. W. V. Hamersvelt, J. M. Wolterink, T. Leiner, M. A. Viergever, and I. Išgum: IEEE Trans. Med. Imaging **38** (2018) 1588. https://doi.org/10.1109/TMI.2018.2883807
25 Y. Jin, Q. Dou, H. Chen, L. Yu, J. Qin, C. Fu, and P. Heng: IEEE Trans. Med. Imaging **37** (2018) 1114. https://doi.org/10.1109/TMI.2017.2787657
26 D. Tellez, M. Balkenhol, I. Otte-Höller, R. V. D. Loo, R. Vogels, P. Bult, C. Wauters, W. Vreuls, S. Mol, N. Karssemeijer, G. Litjens, J. V. D. Laak, and F. Ciompi: IEEE Trans. Med. Imaging **37** (2018) 2126. https://doi.org/10.1109/TMI.2018.2820199
27 D. Allman, A. Reiter, and M. A. L. Bell: IEEE Trans. Med. Imaging **37** (2018) 1464. https://doi.org/10.1109/TMI.2018.2829662
28 P. Naylor, M. Laé, M. Reyal, and T. Walter: IEEE Trans. Med. Imaging **38** (2018) 448. https://doi.org/10.1109/TMI.2018.2865709

29 Y. Wang, H. Dou, X. Hu, L. Zhu, X. Yang, M. Xu, J. Qin, P. Heng, T. Wang, and D. Ni: IEEE Trans. Med. Imaging **38** (2019) 2768. https://doi.org/10.1109/TMI.2019.2913184
30 W. Zhou, H. Li, and M. A. Anastasio: IEEE Trans. Med. Imaging **38** (2019) 2456. https://doi.org/10.1109/TMI.2019.2911211
31 X. Fu, X. Yang, F. Chen, and X. Li: J. Electron. Inf. Technol. **42** (2020) 1782. https://doi.org/10.11999/JEIT190580
32 Y. Li, J. Chen, D. Wei, Y. Zhu, J. Wu, J. Xiong, Y. Gang, W. Sun, H. Xu, T. Qian, K. Ma, and Y. Zheng: IEEE J. Biomed. Health. **26** (2022) 172. https://doi.org/10.1109/JBHI.2021.3119325

About the Author

Shaohu Gu received his M.S. degree from Shenyang Aerospace University, China, in 2015. He joined Changsha Aeronautical Vocational and Technical College, where he is currently a teacher. His research interests include digital image processing and electronic information technology.(shaohugu@163.com)